Daytime convective development over land: A model intercomparison based on LBA observations

By W. W. GRABOWSKI[1]*, P. BECHTOLD[2], A. CHENG[3], R. FORBES[4], C. HALLIWELL[4], M. KHAIROUTDINOV[5], S. LANG[6], T. NASUNO[7], J. PETCH[8], W.-K. TAO[6], R. WONG[8], X. WU[9] and K.-M. XU[3]

[1]*NCAR, Boulder, Colorado, USA*
[2]*ECMWF, Reading, UK*
[3]*NASA Langley Research Center, Hampton, Virginia, USA*
[4]*Met Office JCMM, Reading, UK*
[5]*CSU, Fort Collins, Colorado, USA*
[6]*NASA Goddard Space Flight Center, Greenbelt, Maryland, USA*
[7]*FRCGC, JAMSTEC, Yokohama, Japan*
[8]*Met Office, Exeter, UK*
[9]*ISU, Ames, Iowa, USA*

SUMMARY

This paper investigates daytime convective development over land and its representation in single-column models (SCMs) and cloud-resolving models (CRMs). A model intercomparison case is developed based on observations of the diurnal cycle and convection during the rainy season in Amazonia. The focus is on the 6 h period between sunrise and early afternoon which was identified in previous studies as critical for the diurnal cycle over summertime continents in numerical weather prediction and climate models. This period is characterized by the formation and growth of a well-mixed convective boundary layer from the early morning temperature and moisture profiles as the surface sensible- and latent-heat fluxes increase after sunrise. It proceeds with the formation of shallow convective clouds as the convective boundary layer deepens, and leads to the eventual transition from shallow to deep precipitating convection around local noon. To provide a benchmark for other models, a custom-designed set of simulations, applying increasing in time computational domain and decreasing spatial resolution, was executed. The SCMs reproduced the previously identified problem with premature development of deep convection, less than two hours after sunrise. The benchmark simulations suggest a possible route to improve SCMs by considering a time-evolving cumulus entrainment rate as convection evolves from shallow to deep and the cloud width increases up to an order of magnitude. The CRMs featuring horizontal grid length around 500 m are capable of capturing the qualitative aspects of the benchmark simulations, but there are significant differences among the models. Two-dimensional CRMs tend to simulate too rapid a transition from shallow to deep convection and too high a cloud cover.

KEYWORDS: Boundary layer   Diurnal cycle   Moist convection

1. INTRODUCTION

In terms of energy fluxes across the atmosphere, the diurnal cycle of solar radiation provides the strongest external forcing on the climate system. Through their influence on radiative fluxes, clouds exert a significant impact on the diurnal cycle of various meteorological variables. At night, clouds trap thermal radiation (the greenhouse effect) and thus warm the surface. During the day, on the other hand, clouds reflect solar energy back to space and thus cool the surface. Because of the small heat capacity of the land surface compared to the ocean, the diurnal cycle is particularly strong over summertime continents, where convective processes play a crucial role in distributing the energy and water across the atmosphere. These processes occur on a wide range of temporal and spatial scales, from tens of metres (e.g. dry convection within the convective boundary layer or coherent structures within the night-time stable boundary layer) to hundreds of kilometres (e.g. mesoscale convective systems).

Because of the range of spatial scales involved and complicated interactions among various physical processes (radiative, transport, phase change, etc.), representing the

---

diurnal cycle in large-scale models of weather and climate poses a difficult challenge (see Guichard *et al.* 2004, hereafter G2004; Bechtold *et al.* 2004, hereafter B2004, and references therein). As documented by Yang and Slingo (2001), Betts and Jakob (2002a) and G2004, the problem is particularly severe over summertime continents and is highlighted by the anomalous diurnal cycle of surface precipitation, which tends to peak up to several hours too early in models compared to observations. This problem was investigated in detail in G2004, where a model intercomparison case was developed based on observations over the Atmospheric Radiation Measurement (ARM) Program Southern Great Plains (SGP) Clouds And Radiation Testbed (CART) site in Oklahoma. This observationally based case was part of the European Cloud Systems (EUROCS) project and it involved simulations by single-column models (SCMs) and cloud-resolving models (CRMs). One of the conclusions of the investigation reported in G2004, previously shown true for the European Centre for Medium-Range Weather Forcasts (ECMWF) model (Betts and Jakob 2002a), was that SCMs tend to develop deep convection too rapidly, without the shallow convection phase and gradual transition from shallow to deep convection.

This paper reports on results of the investigation that builds upon the G2004 and B2004 studies and involves several members of Working Group 4 (Precipitating Convective Cloud Systems) of the GCSS (GEWEX Cloud System Study: GEWEX stands for Global Energy and Water Cycle Experiment, see http://www.gewex.org/). The study investigates the daytime convective development over land, which starts with a formation and growth of a convective boundary layer from the early morning sounding, proceeds with formation of shallow convective clouds as the convective boundary layer deepens, and leads to eventual transition from shallow to deep precipitating convection. The investigation focuses only on a part of the diurnal cycle (from the sunrise to early afternoon) which was shown in G2004 and B2004 to be the most difficult to capture in the large-scale models of weather and climate. The study involves both SCMs and CRMs, and the intercomparison case is based on observations during the Large-Scale Biosphere–Atmosphere (LBA) experiment in Amazonia (Rondonia, Brazil) with specific data collected during the Tropical Rainfall Measuring Mission, LBA ground validation program (TRMM-LBA), on 23 February 1999.

The overall strategy of the investigation reported herein is (i) to develop a model intercomparison case which features essential observed characteristics of the daytime convective development over land; (ii) to perform a benchmark simulation using spatial resolution sufficient to capture the observed characteristics; (iii) to compare the benchmark to results from SCMs and CRMs in their standard configurations. The latter phase allows identification of areas that need attention in future developments of SCMs and CRMs.

The next section discusses the convection over the LBA area and provides details required for numerical simulations of this case. Section 3 describes the benchmark set of simulations that serves as a basis for the model intercomparison presented in sections 4, 5 and 6. Discussion and conclusions follow in section 7.

2.   THE MODEL INTERCOMPARISON BASED ON 23 FEBRUARY 1999 TRMM-LBA OBSERVATIONS

(a)   *Convection over LBA area and the 23 February 1999 case*

Deep convection over the LBA area falls into two general regimes (e.g. Rickenbach *et al.* 2002 and references therein). The break-type convection, often featuring fast-propagating mesoscale convective systems (squall lines), occurs during periods with

easterly lower tropospheric flow. During periods with westerly flow in the lower half of the troposphere, monsoon-type convection occurs and is dominated by widespread popcorn-type deep convection. The latter regime features weaker mesoscale organization and strong diurnal cycle. The 23 February 1999 case occurred during the monsoon-type regime. This is one of the cases discussed in Betts *et al.* (2002).

The daytime convective development over LBA features formation of a well-mixed convective boundary layer from the early morning sounding, subsequent initiation of shallow convection as the boundary layer deepens, transition from shallow to deep convection around local noon, and organization of convection into mesoscale features in the afternoon (see a discussion in Betts *et al.* (2002) and references therein; see also a library of TRMM-LBA S-Pol radar scans available at http://www.atd.ucar.edu/rsf/TRMM-LBA/quicklook/spol_trm.htm). The mesoscale organization stage is most likely strongly affected by the day-to-day variability of synoptic conditions (e.g. profiles of shear, stability, moisture), mesoscale features, and local topography, but the first three phases seem quite universal (cf. Betts *et al.* 2002, Figs. 5 and 6).

Inspection of the radar data available at the TRMM-LBA website for the 23 February 1999 shows the presence of night-time stratiform echoes (with radar reflectivity maxima below 25 dBz) around sunrise (0730 LST, LST = UTC − 4 h) which dissipate over the next two hours. The first convective echoes develop around 1030 LST (i.e. 3 hours after sunrise). Over the next two hours their aerial coverage increases rapidly to cover a significant part of the radar scene by 1230 LST. Mesoscale organization into north-west to south-east oriented bands becomes apparent by 1330 LST (i.e. 6 hours after sunrise) and these bands evolve into widespread stratiform echoes by the early evening hours. The study reported here focuses on convective development prior to the mesoscale organization using the integration window for the models between sunrise and 1330 LST.

(b) Case specification

This case does not feature any 'large-scale' forcing, i.e. no advective tendencies of temperature and moisture are specified as the simulation progresses. The only forcing comes from evolving surface fluxes and evolving tendencies due to radiative processes, both prescribed (and thus identical) for each model involved in the intercomparison. The initial sounding (at 0730 LST) and the evolutions of surface fluxes and temperature tendencies due to radiative processes are given in the appendix (also available at http://box.mmm.ucar.edu/gcss-wg4/model/intercomp.html).

Numerical simulations are initiated using the morning sounding and are forced by evolving surface fluxes and radiative cooling. The mean horizontal wind is relaxed to the initial profile using a 1 h relaxation time-scale. For CRMs, lateral boundary conditions are periodic and small-scale random perturbations are imposed to excite instabilities throughout the simulation. The latter involve random perturbations on surface temperature and moisture fluxes (with the 10% amplitude and random numbers generated every time step) and random perturbations added to the temperature and moisture fields, with amplitudes of 0.1 K and 0.1 g kg^{-1}, applied in the lowest 1 km every 15 min. Two-dimensional CRMs are aligned east–west.

3. BENCHMARK ENSEMBLE OF MODEL SIMULATIONS

(a) Model set-up

The numerical model applied in the benchmark ensemble simulations is the massively parallel version (Anderson *et al.* 1997) of the two-time-level, non-hydrostatic
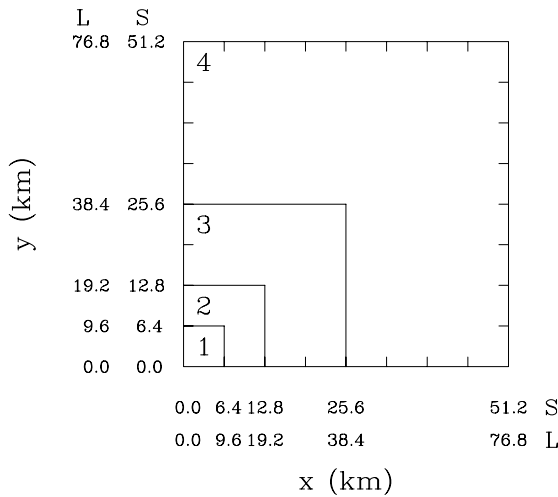
Figure 1.   Extent of computational domains in the horizontal plane in benchmark simulations. Each simulation starts using domain marked as 1 and finishes with the domain marked as 4. The remapping procedure is applied three times, from domain 1 to 2, from 2 to 3, and from 3 to 4. The numbers along horizontal and vertical axes show the extent (in kilometres) of the domains in simulations S and L.

Eulerian/semi-Lagrangian anelastic fluid model EULAG of Smolarkiewicz and Margolin (1997), with the moist precipitating thermodynamics applied as discussed in Grabowski and Smolarkiewicz (1996) and in Grabowski (1998). The Eulerian variant of EULAG is used.

To resolve the range of spatial and temporal scales involved in the development of convective boundary layer and transition from shallow to deep convection, we follow a modelling strategy used by Müller and Chlond (1996) in their simulation of the boundary-layer development in cold-air outbreaks. The strategy involves applying a small computational domain and high spatial resolution (typical of large-eddy simulation approach) to represent the development of a convective boundary layer and shallow convection in the early part of the simulation. At later times, a remapping procedure increases the computational domain and the grid length towards those applied in cloud-resolving simulations.

In Müller and Chlond (1996), a decision when to apply the remapping procedure to increase the domain size and reduce spatial resolution was based on the evolution of the wave-number spectrum of the kinetic energy. Herein, the decision is made by monitoring the increase of the boundary-layer depth and the increase in the horizontal and vertical extent of clouds. The time of the remapping is varied in two sets of model simulations. In each set, two simulations are performed using a different number of points in the horizontal plane. Such an approach leads to a four-member ensemble of simulations which are used as a benchmark for SCMs and CRMs. By comparing solutions for ensemble members, a posteriori evaluation of the effect of the remapping procedure on the results is possible.

The simulations are performed in the following manner (see Figs. 1, 2 and 3, as well as Table 1). We start with high spatial resolution (50 and 25 m horizontal and vertical grid spacing, respectively) using a computational domain of $128 \times 128 \times 161$ (simulation S1: S for Small horizontal domain) and $192 \times 192 \times 161$ (simulation L1: L for Large horizontal domain), see Figs. 1 and 2. The computational domain,
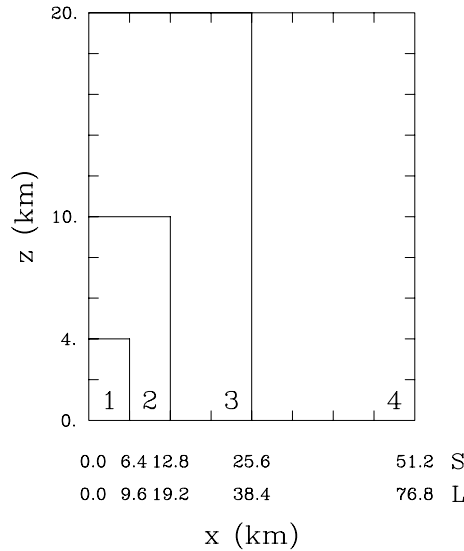
Figure 2.   Similar to Fig. 1, but for the extent of computational domains in the vertical plane.
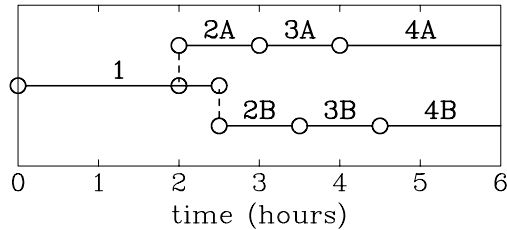

Figure 3.   Timeline of the ensemble of benchmark simulations. The numbers correspond to the computational domains shown in Figs. 1 and 2. The simulations start at $t = 0$ using computational domain typical for LES modelling, and finish at $t = 6$ h using computational domain large enough for an ensemble of deep convective clouds. Simulations marked as A apply the remapping procedure at $t = 2$, 3 and 4 h to obtain domains shown as 2, 3 and 4 in Figs. 1 and 2. Simulations marked as B apply the same procedure at $t = 2.5$, 3.5 and 4.5 h. Because the two sets are applied with two different numbers of grid points in the horizontal plane (set S is 128×128; set L is 196×196), an ensemble of four simulations is obtained.

TABLE 1.   LIST OF BENCHMARK SIMULATIONS

Simulation code	$\Delta x\ (= \Delta y)$ (m)	$L_x\ (= L_y)$ (km)	Δz (m)	N_z	L_z (km)	Start time (h)	End time (h)	Started from
S1, L1	50	6.4, 9.6	25	161	4.0	0.0	2.5	
S2A, L2A	100	12.8, 19.2	50	201	10.0	2.0	3.0	S1, L1
S2B, L2B	100	12.8, 19.2	50	201	10.0	2.5	3.5	S1, L1
S3A, L3A	200	25.6, 38.4	100	201	20.0	3.0	4.0	S2A, L2A
S3B, L3B	200	25.6, 38.4	100	201	20.0	3.5	4.5	S2B, L2B
S4A, L4A	400	51.2, 76.8	100	201	20.0	4.0	6.0	S3A, L3A
S4B, L4B	400	51.2, 76.8	100	201	20.0	4.5	6.0	S3B, L3B

Set S (L) = 128×128 (196×196) horizontal domain; L_x, L_y, L_z = extent of the computational domain in horizontal and vertical directions; Δx, Δy = horizontal grid lengths; Δz = vertical grid length; N_z = number of model levels. In the third and the ninth column, the first entry is for the set S, and the second for the set L.

6.4(S1)/9.6(L1) km in the horizontal and 4 km in the vertical, is large enough to represent development of convective boundary layer and shallow convective clouds in the first 3 h of the simulations. To capture further development of convection, a larger horizontal domain (in both horizontal and vertical) is needed. The domain appropriate for an ensemble of deep convective clouds, i.e. covering the entire troposphere and extending several tens of kilometres in both horizontal directions, is reached by performing three times a remapping procedure similar to that used by Müller and Chlond (1996) (see Fig. 3 for the timeline of benchmark simulations). In this procedure, higher-resolution fields at a given time are appropriately averaged to provide lower spatial resolution data needed to restart the model using a larger computational domain. The fact that the model applies periodic lateral boundaries is essential.

The procedure to create lower-resolution fields to be applied in larger-domain simulation is as follows. In the horizontal plane, original higher-resolution fields are spatially averaged to obtain lower-spatial-resolution fields, which are applied in four quadrants of a horizontal domain four times larger than the original one (cf. Fig. 1). The new horizontal domain is covered by the same number of grid points and the horizontal grid spacing is twice as large as in the original fields. Because of a particular realization of periodic lateral boundary conditions in EULAG, the averaging scheme produces four slightly different copies of lower horizontal resolution data in four quadrants of the larger horizontal domain. In the vertical, the remapping from higher to lower vertical resolution involves a similar averaging procedure (cf. Fig. 2). Because this is only possible in the part of the lower-resolution domain which covers the original higher-resolution domain, horizontally homogeneous fields based on the initial sounding are applied in the extended part of the lower-resolution vertical domain.

The remapping procedure is applied first at 2.0 and 2.5 h to start four sets of simulations (S2A and S2B starting from S1 and L2A and L2B starting from L1, cf. Fig. 3). These simulations apply horizontal and vertical grid spacing of 100 and 50 m, respectively. Each of these simulations is advanced 1 h and the remapping procedure is repeated. The next set of four simulations (S3A and S3B starting from S2A and S2B, respectively; L3A and L3B starting from L2A and L2B) apply horizontal and vertical grid spacing of 200 and 100 m, respectively. These simulations are again advanced by 1 h and a final remapping is performed, only in the horizontal. The final set of simulations (S4A and L4A starting at 4 h, but S4B and L4B starting at 4.5 h) is performed up to $t = 6$ h. All simulations apply a 3 s time step, except for the final half an hour of high-resolution simulations S1 and L1 which require a 2 s time step for numerical stability. Simulation details are summarized in Table 1.

(b)   Results

Figure 4 shows the evolution of the horizontally averaged lower-tropospheric temperature and moisture profiles during the course of ensemble simulations. After the first hour, surface heating produces a shallow (about 100 m deep) well-mixed boundary layer. Small clouds appear near the top of the boundary layer between hour 1 and 2 (cf. Fig. 6). At $t = 2$ h, the well-mixed layer is about 300 m deep, but the effects of clouds extend to almost 500 m as evident by the perturbation moisture profile. Note that the air above the mixed layer is more humid and colder than the original profiles. This is most likely associated with the detrainment and evaporation of cloud condensate during the shallow convection phase. Such changes of the profiles are also evident at $t = 3$ h, where the temperature perturbation profile suggests about a 500 m deep boundary layer and the effects of clouds extend way above 1 km (cf. Fig. 6). The warming of the air above the boundary layer associated with deep convective heating is evident in

a) potential temperature profiles (K)
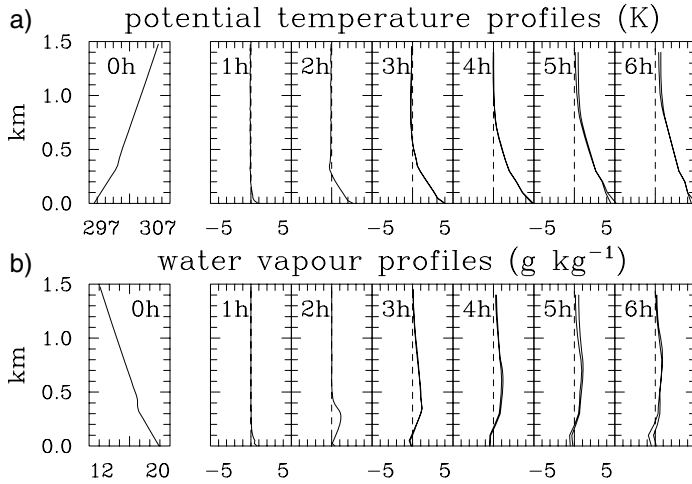

b) water vapour profiles (g kg^{-1})

Figure 4. Evolution of the lower-tropospheric (a) potential-temperature and (b) water-vapour mixing-ratio profiles for four benchmark simulations. The profiles are plotted as deviations from the initial profiles to better expose the changes due to boundary-layer and cloud processes.

temperature profiles at hours 5 and 6. Convective downdraughts, which bring colder and drier air from the free troposphere into the boundary layer, modify the near-surface profiles starting at $t = 3$ h. This is especially pronounced in the moisture profiles.

Figure 5 shows evolutions of the total cloud cover and the height of the centre of mass of the cloud field derived from the ensemble of simulations. The total cloud cover is defined as the fraction of columns classified as cloudy, where a column is considered cloudy if the vertically integrated concentration of cloud condensate (i.e. cloud water plus cloud ice) is larger than 0.01 kg m^{-2}. The height of the centre of mass is defined as $\int zQ \, dV / \int Q \, dV$, where Q is the mixing ratio of total condensed water (i.e. cloud condensate and precipitation), z is the vertical coordinate, V is volume, and integration is over the entire computational domain. The evolution of cloud cover shows considerable scatter among the ensemble simulations, with some impact of the remapping procedure evinced by rapid decrease of cloud cover immediately after the remapping at hour 2.0, 2.5, 3.0, 3.5, etc. Some scatter also comes from the inherently stochastic nature of convection (i.e. different realizations are characterized by different cloud covers as the depth of the cloud field increases, see a discussion in Petch (2005)). Similar scatter is also observed in other results of the benchmark simulations (e.g. surface precipitation or convective mass flux). In general, cloud cover increases steadily between $t = 2$ h and the end of simulations (from about 0.1 to around 0.5). The evolution of the centre of mass of the cloud field shows significant scatter only in the final two hours of the benchmark simulations. The centre of mass rises steadily from about 0.5 km at 2 h (i.e. shallow clouds) to about 7 km at the end of simulations, suggesting that clouds fill the entire depth of the troposphere at the final stages of the simulations.

Figure 6 shows the evolution of the cloud fraction profiles. The cloud fraction is defined as a fraction of grid boxes at a given level with the cloud condensate mixing ratio larger than the threshold value, selected as min(10^{-5}, $0.01q_{vs}$), where q_{vs} is the saturated water-vapour mixing ratio. Based on the evolution of the centre of mass of the cloud field (Fig. 5) and cloud fraction profiles (Fig. 6), the period prior to 3 h can be
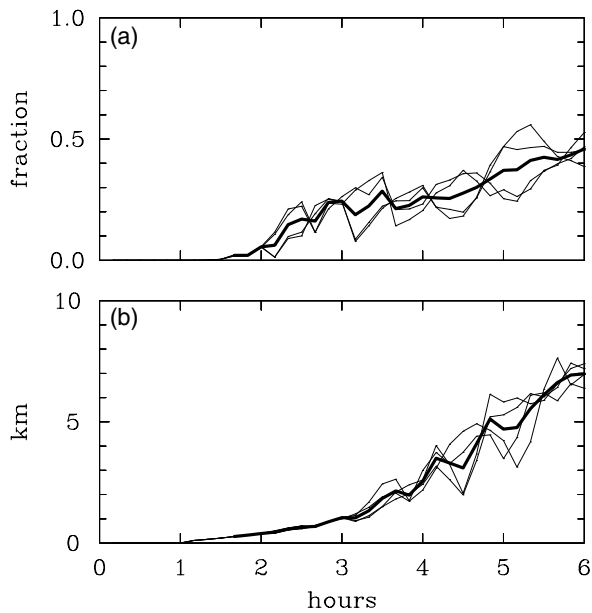
Figure 5. Evolution of (a) the total cloud cover and (b) the height of the centre of mass of the cloud field (both defined in text) for the four benchmark simulations. The ensemble means are shown using thick lines.
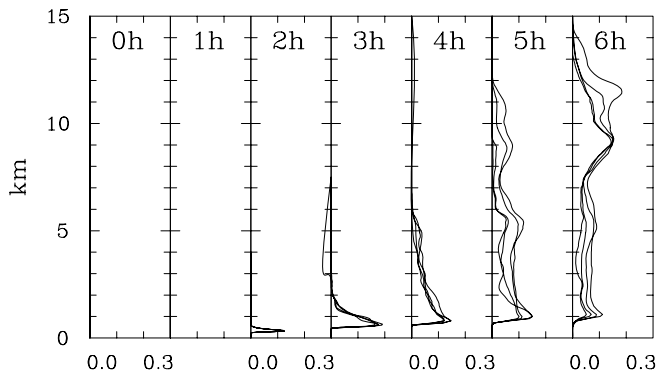

Figure 6. Evolution of the instantaneous cloud-fraction profiles for the four benchmark simulations.

referred to as shallow convection, and after 5 h as deep convection. The period between 3 and 5 h is the shallow-to-deep-convection transition.

As Fig. 6 illustrates, the cloud base tends to rise as the day progresses, which is a typical feature of convective development over land (cf. Brown *et al.* 2002, Fig. 5(c); Betts *et al.* 2002, Fig. 5; Betts and Jakob 2002a, Fig. 2). The rise of the cloud base results from a gradual decrease of the near-surface relative humidity from morning to early-afternoon hours (the surface relative humidity in the benchmark simulations decreases from about 95% at $t = 0$ to about 70% at $t = 6$ h). The cloud-fraction profiles show little scatter among ensemble members up to 4 h, and significant scatter at $t = 5$ and 6 h. The increase of the upper-tropospheric cloud fraction in the final hour of the
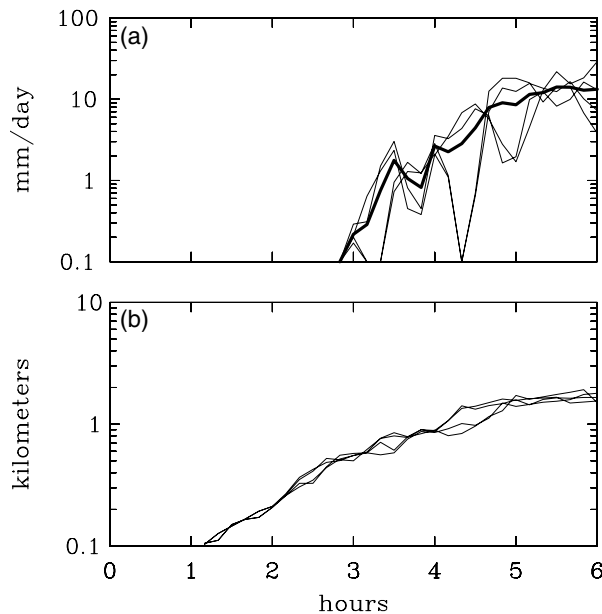
Figure 7. Evolution of (a) the 10 min averaged surface precipitation rate and (b) the mean cloud width, for four benchmark simulations. The thick solid line in (a) shows evolution of the ensemble-mean surface precipitation rate.

simulations is due to the development of stratiform outflow anvil clouds associated with deep convection.

The change of the cloud-top height during the shallow-to-deep convection transition between hours 3 and 5, from about 2 km to about 12 km (cf. Fig. 6), implies the rate of rise of about 1.5 m s^{-1}. During this period, the maximum vertical velocities inside clouds increases from below 5 m s^{-1} at $t = 3$ h to about 10 m s^{-1} at $t = 4$ h, and about 15 m s^{-1} at $t = 5$ h (not shown). Consequently, the transition is unlikely to be associated with growth of a single set of clouds from shallow to deep because such a growth would imply a faster transition considering the magnitude of updraught velocities inside clouds. More likely, clouds developing later in the transition period attain higher altitudes until they eventually reach the upper troposphere around $t = 5$ h. This is supported by the inspection of the evolution of individual clouds in benchmark simulations (not shown).

Figure 7 shows evolutions of the 10 min averaged surface precipitation rates and the averaged cloud width throughout the benchmark simulations. The averaged cloud width is defined in the following way. First, the lengths of all cloud transects along a 'flight track' at $x = 0$ and at the height of the maximum cloud fraction near the cloud base (cf. Fig. 6) are calculated. By repeating this procedure for all x and then selecting the flight tracks along the x-axis (i.e. for all y), a set of all cloud transects is obtained. The averaged cloud width is defined as the mean of the set*. This procedure is applied to all ensemble members.

* When sampled according to this procedure, the mean length of a transect for a circular well-resolved cloud base is approximately equal to $1.5R$ (where R is the radius of the cloud base), and not $2R$ as one would take as a cloud width. For poorly resolved clouds, however, the mean length of a transect will be approximately equal to the cloud base width. For 2D simulations discussed later in the paper, the transect length is the width of a cloud.
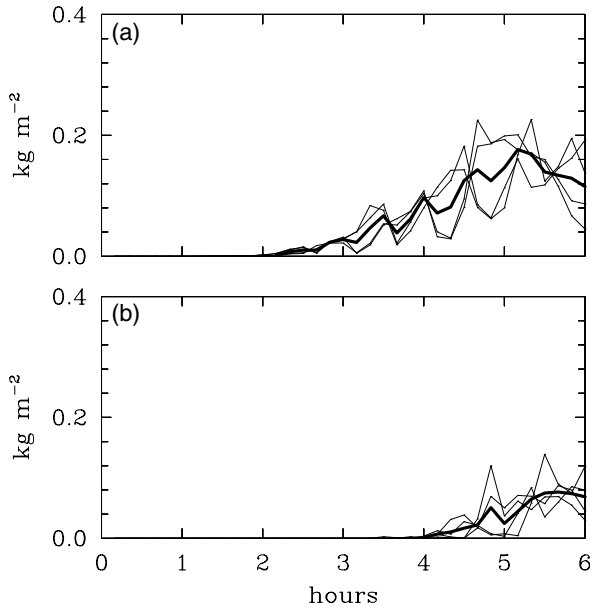
Figure 8.   As Fig. 5, but for (a) the liquid-water and (b) the ice-water paths.

The surface precipitation rate (Fig. 7(a)) shows considerable scatter due to the stochastic nature of convection and rather small domain size from the deep convection point of view, especially during the shallow-to-deep-convection transition (cf. Petch 2005). The overall evolution of the mean surface precipitation rate shows that the averaged values of about 0.1 mm d^{-1} are reached at about $t = 3$ h and the mean rate of the order of 10 mm d^{-1} occurs in the last hour of the simulations. The mean cloud width (Fig. 7(b)) increases rapidly during the second and third hours of simulation, from about 100 m when clouds first appear to about 600 m at $t = 3$ h. This increase is slightly faster than the increase of the boundary-layer depth which changes from about 100 m at $t = 1$ h to less than 500 m by $t = 3$ h. The mean cloud width at the end of simulations approaches 2 km and it is still slowly increasing.

Figure 8 shows the evolution of the horizontally averaged liquid- and ice-water paths. Although, as in Fig. 5, the scatter is considerable, the transition from shallow to deep convection is associated with an increase of the mean liquid-water path from a few tens of g m^{-2} to values in the 100 to 200 g m^{-2} range. The ice-water path is negligible prior to $t = 4$ h and reaches values in the range of 50 to 100 g m^{-2} towards the end of the simulations.

Finally, Fig. 9 shows the evolution of updraught and downdraught cloud mass fluxes for all four benchmark simulations. Cloud updraught mass flux at any level is defined as the horizontal average of $\delta\rho \max(0, w)$, where ρ is the air density, w is local vertical velocity, and $\delta = 1$ if the cloud condensate mixing ratio is larger than the threshold value, $\min(10^{-5}, 0.01q_{vs})$, and $\delta = 0$ otherwise. Cloud downdraught mass flux at any level is defined as the horizontal average of $\delta\rho \min(0, w)$, where $\delta = 1$ if the cloud condensate mixing ratio is larger than the same threshold value or the precipitation mixing ratio is larger than 10^{-4}; $\delta = 0$ otherwise. In general, the updraught mass-flux profiles are well correlated with the cloud-fraction profiles shown in Fig. 6 (except for the upper-tropospheric clouds at $t = 6$ h). Downdraught mass fluxes are weak prior to $t = 4$ h and
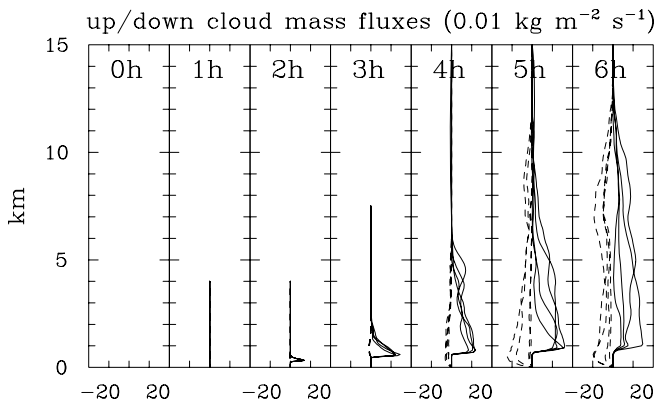
Figure 9. Evolution of the updraught (solid lines) and downdraught (dashed lines) cloud mass-flux profiles averaged over the four benchmark simulations.

TABLE 2. SINGLE-COLUMN MODELS PARTICIPATING IN THIS INTERCOMPARISON STUDY

Model	ECMWF SCM	UKMO SCM
Modeller	Bechtold	Wong
References	Tiedtke (1989) Bechtold *et al.* (2004)	Gregory and Rowntree (1990) Pope *et al.* (2000)
Shallow convection scheme	Mass flux; moist static energy equilibrium closure	Gregory–Rowntree mass-flux scheme, CAPE closure
Deep convection scheme	Mass flux; CAPE closure; fixed turbulent and variable organized (moisture convergence) entrainment	Gregory–Rowntree mass-flux scheme, CAPE closure
Boundary-layer scheme	K-diffusion (up to cloud base)	K-profile scheme (Lock *et al.* 2000)

the scatter of the fluxes for $t = 5$ and 6 h is significant. The former agrees with the notion that precipitation mass loading and its evaporation is the main driving mechanism for convective downdraughts. It is also evident from Fig. 9 that the transition from shallow to deep convection is associated with a rather small increase of the updraught mass flux near the cloud base and a significant increase (in the absolute sense) of the cloud-base downdraught mass flux.

4. MODELS PARTICIPATING IN THE INTERCOMPARISON

The intercomparison involves several CRMs and two SCMs, both of which are operational in full 3D large-scale models. Tables 2 to 5 provide relevant information about the models and details of the simulations performed.

5. SINGLE-COLUMN MODEL SIMULATIONS

Before discussing the SCM results, it should be pointed out that despite the short integration period, typically characterized by the so-called model 'spin-down' (i.e. maximum surface precipitation occurring close to the initial time), the case discussed in this

TABLE 3.   CLOUD-RESOLVING MODELS PARTICIPATING IN THIS INTERCOMPARISON STUDY

Model	Model full name	Modeller(s)	Reference(s)
CRCP	Cloud-Resolving Convection Parametrization	Grabowski	Grabowski (2001, 2003)
EULAG	NCAR EUlerian/semi-LAGrangian small-scale model	Grabowski	Smolarkiewicz and Margolin (1997) Grabowski (1998)
GCE	Goddard Cumulus Ensemble Model	Lang and Tao	Tao and Simpson (1993) Tao *et al.* (2003)
ISU-CRM	Clark/Hall cloud model	Wu	Clark *et al.* (1996) Wu and Moncrieff (2001)
JMA	JMA Unified Nonhydrostatic Model	Nasuno	Saito *et al.* (2001)
LaRC	University of California, Los Angeles/ NASA Langley Research Center small-scale model	Cheng and Xu	Krueger (1988) Xu and Krueger (1991)
MOUM	UK Met Office Unified Model	Halliwell and Forbes	Davies *et al.* (2005), Wilson and Ballard (1999)
SAM	System for Atmospheric modelling	Khairoutdinov	Khairoutdinov and Randall (2003)
UKLEM	UK Met Office Large-Eddy Model	Petch	Shutts and Gray (1994) Swann (1998)

JMA is Japan Meteorological Agency. Unlike all other models, GCE applied interactive radiation transfer model.

paper is a valid test for SCMs. For instance, many (diagnostic) convective parametrization schemes are based on the quasi-equilibrium assumption, where convection quickly (often instantaneously) adjusts to changes in the large-scale conditions. The daytime convective development is a situation where such an approach is expected to be problematic because the rapid evolution of surface fluxes and the gradual rise in the convective layer (one wishes to resolve) make the quasi-equilibrium assumption questionable.

The two SCMs that simulated the case discussed in this paper experienced the same difficulties in representing convective development as observed in other studies of the diurnal cycle over land, e.g. Yang and Slingo (2001), Betts and Jakob (2002a) and B2004, G2004. In both ECMWF and United Kingdom Met Office (UKMO) SCM, surface precipitation rate reaches values of more than 10 mm d^{-1} during the second hour of the simulation and the precipitation rate fluctuates between 10 and 40 mm d^{-1} throughout the rest of the simulations (not shown). Nevertheless, evolution of the lower-tropospheric temperature and moisture profiles resembles those in the benchmark simulations, as illustrated in Fig. 10. This is particularly true for the temperature profiles, which show development of a convective boundary layer quite similar to that in the benchmark simulation shown in Fig. 4 (however, the difference between the two SCM temperature profiles increases as the simulations progress). Moisture profiles, on the other hand, differ more significantly, with ECMWF SCM showing a stronger effect of convective downdraughts.

The rapid onset of deep convection in SCMs is evident in the profiles of cloud fraction shown in Fig. 11 and cloud updraught and downdraught mass fluxes shown in Fig. 12. For the UKMO SCM, cloud-fraction profiles reach overcast in the upper troposphere during the second hour and such conditions are maintained throughout the remainder of the simulation. These high values are presumably associated with parametrized convective outflow anvils. The lower-tropospheric values are quite realistic

TABLE 4. MODEL FORMULATION AND NUMERICAL TECHNIQUES

Model	Geometry	Dynamics	Thermodynamics	Time differencing	Momentum/scalar advection	Turbulence scheme	Boundary-layer scheme
CRCP	2D	Anelastic	Warm-rain, simple ice	NFT, 2nd order	Monotone, 2nd order	None	Non-local (Troen and Mahrt 1986)
EULAG	3D	Anelastic	Warm-rain, simple ice	NFT, 2nd order	Monotone, 2nd order	S-type	None
GCE	3D	Compressible	Warm-rain, 3 classes of ice	Leapfrog/NFT	2nd order	TKE, 1.5 order	None
ISU-CRM	2D	Anelastic	Warm-rain 2 classes of ice	Leapfrog/NFT	2nd order, monotone for scalars	S-type	Non-local (Troen and Mahrt 1986)
JMA	2D/3D	Compressible	Warm-rain, 3 classes of ice (Ikawa et al. 1991)	Semi-implicit, leapfrog with time filter	2nd order	TKE-type, 1.5 order (Saito 1993)	None
LaRC	2D	Anelastic	Warm-rain, SGS condensation (Sommeria and Deardorff 1977)	A-B 2nd order	2nd order	Prognostic 3rd order closure	None
MOUM	3D	Compressible	Prognostic liquid water and ice (Wilson and Ballard 1999)	1st order, two-time level, semi-implicit predictor-corrector (Davies et al. 2005)	2nd order, semi-Lagrangian	'Targeted diffusion'	K-profile scheme (Lock et al. 2000)
SAM	3D	Anelastic	Diagnostic cloud water and ice, rain, gaupel, snow	A-B, 3rd order	Monotone, 2nd order	S-type	None
UKLEM	2D/3D	Anelastic	Warm-rain, three classes of ice	Leapfrog/ forward	2nd order	S-type	None

A–B = Adams–Bashforth; NFT = Non-oscillatory Forward-in-Time (Smolarkiewicz and Grabowski 1990); S-type = Smagorinsky-type; SGS = subgrid-scale; 'targeted diffusion' = diffusion applied only in the vicinity of excessive vertical velocities; TKE = turbulent kinetic energy.

TABLE 5.   LIST OF CRM SIMULATIONS

Model	Simulation	$L_x \times L_y \times L_z$ or $L_x \times L_z$ if 2D	$\Delta x, \Delta y$ or Δx if 2D	Δz or N_z if stretched	Δt (s)
CRCP	2D	200 km ×24 km	2 km	61 levels	15
EULAG	3D	64 km × 64 km × 20 km	500 m	125 m	4
GCE	3D-LR	64 km × 64 km × 22 km	1 km	41 levels	10
	3D-HR	64 km × 64 km × 22 km	250 m	41 levels	5
ISU-CRM	2D	200 km × 40 km	3 km	52 levels	15
JMA	3D	150 km × 150 km × 21 km	500 m	76 levels	5
	2D	250 km × 21 km	500 m	76 levels	5
LaRC	2D-LR	256 km × 20 km	1 km	100 m	2
	2D-HR	256 km × 20 km	100 m	100 m	2
MOUM	3D	100 km × 100 km × 30 km	1 km	73 levels	30
SAM	3D-LR	120 km × 120 km × 24 km	500 m	56 levels	10
	3D-HR	154 km × 154 km × 25 km	100 m	256 levels	2
UKLEM	3D	10 km × 10 km × 20 km	100 m	199 levels	4
	2D-LR	250 km × 20 km	1 km	199 levels	4
	2D-HR	200 km × 20 km	100 m	199 levels	4

L_x, L_y, L_z = extent of the computational domain in horizontal and vertical directions; Δx, Δy = horizontal grid lengths; Δz = vertical grid length; N_z = number of model levels; Δt = model time step; LR and HR stand for low and high spatial resolution, respectively.
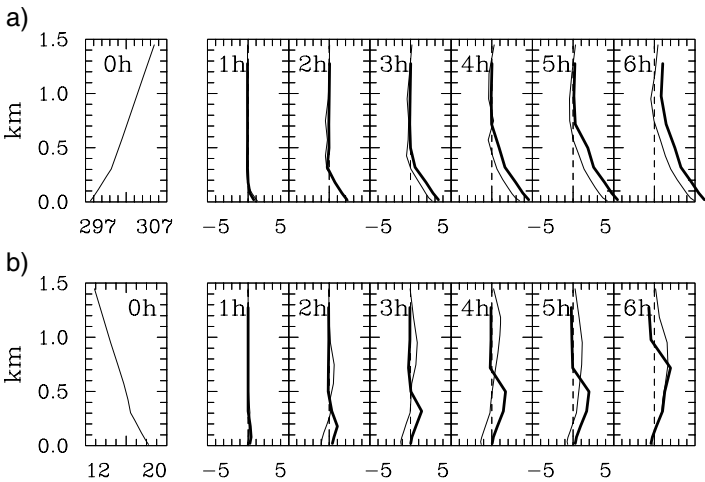

Figure 10.   Evolution of the lower-tropospheric (a) potential-temperature and (b) water-vapour mixing-ratio profiles for ECMWF (thin lines) and UKMO SCMs (thick lines). As in Fig. 4, the profiles are plotted as deviations from the initial profiles.

(around 0.1; cf. Fig. 6 for benchmark). The values for the ECMWF SCM are also realistic across most of the troposphere (with rather weak upper-tropospheric anvils), except for very high values (up to total overcast by $t = 5$ h) near the top of the boundary layer. The latter is most likely due to the shallow convection parametrization and its interaction with other parametrized physics (e.g. boundary layer, deep convection).

Cloud mass fluxes also differ significantly between the two models. The ECMWF model tends to simulate excessive updraught mass fluxes due to shallow convection
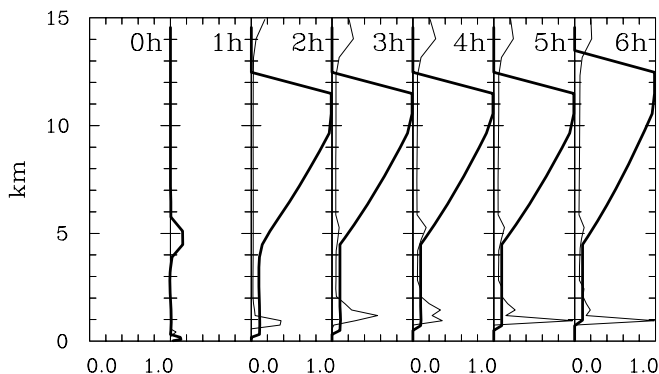
Figure 11.   Evolution of the cloud-fraction profiles for ECMWF (thin lines) and UKMO SCMs (thick lines).
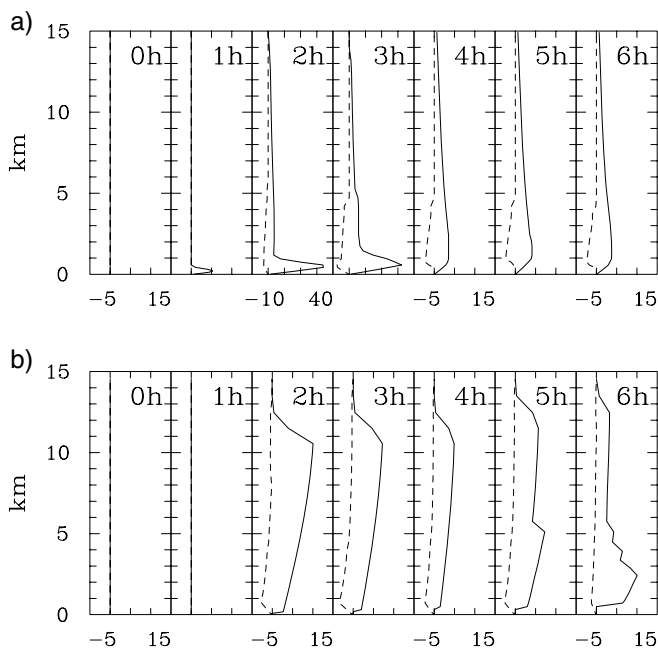

Figure 12.   Evolution of the cloud updraught (solid lines) and downdraught (dashed lines) mass-flux profiles for (a) ECMWF and (b) UKMO SCMs. The scale on the horizontal axis in the ECMWF plot is the same as in the UKMO except for hours 2 and 3 where it is from -10 to 40 (0.01 kg m^{-2}s^{-1}).

at hours 2 and 3 (roughly 3 times as high as in the benchmark case) and decreasing with height mass flux due to deep convection, similar in strength to the deep convection phase of the benchmark. The updraught mass flux in the UKMO SCM changes from top-heavy at hour 2 and 3 to a more realistic bottom-heavy at the end of the simulation. The downdraught mass fluxes in both SCMs are too weak compared to the benchmark, a common problem in many SCM simulations of continental convection (Xie *et al.* 2002).

The central issue is why the two SCMs are not capable of gradual development of a convective boundary layer and shallow convection without the premature appearance of deep convection. One possible explanation is related to the increase of the width of

clouds as the convection changes from shallow to deep as shown by the benchmark. The order of magnitude increase of the cloud width illustrated in Fig. 7 suggests about an order of magnitude decrease of the entrainment rate between shallow and deep convection. Perhaps the rapid development of deep convection in SCMs can be suppressed by a varying entrainment rate throughout the day. The simplest approach might be to make the entrainment rate just a function of a local time during morning hours. More appropriate, however, would be to develop a consistent approach where the cloud width, the depth of convection layer, and the entrainment rate are all either diagnostically or prognostically related during the transition from shallow to deep convection.

6.   CLOUD-RESOLVING MODEL SIMULATIONS

In general, CRMs were more successful in simulating the sequence of events observed over the LBA network and represented in the benchmark simulations. Evolution of most parameters (boundary-layer height, surface precipitation rate, liquid-water and ice paths, cloud cover, centre of mass, etc.) were in qualitative agreement among all the CRMs. However, there were some quantitative differences. The following discussion highlights some of the discrepancies and attempts to relate them to the differences in model formulation (e.g. 3D versus 2D, time integration scheme, etc.), model spatial resolution, or subgrid-scale parametrized physics (e.g. turbulence). Further investigations to better understand deficiencies and reduce discrepancies is beyond the scope of this paper. This task is left for future research by individual modellers.

(a)   3D CRMs

Figures 13 to 16 show evolutions of the surface precipitation rate, the cloud cover, the height of the centre of mass of the cloud field, and the mean cloud width for 3D CRMs. They should be compared with the benchmark results (Figs. 5 and 7). Surface precipitation rate in all 3D models reaches 0.1 mm d^{-1} around $t = 3$ h, except for 1 km horizontal resolution in the GCE model where it is delayed until $t = 4$ h. Such a delay is consistent with the late development of cloudiness in this simulation as illustrated by the evolutions of the cloud cover and the height of the centre of mass. Increasing the horizontal resolution to 250 m improves the GCE simulation considerably.

Simulations shown in Figs. 13(a), 14(a) and 15(a) exhibit some differences compared to the benchmark. MOUM, EULAG and JMA show rapid increase of the surface precipitation around $t = 3$ h; MOUM and JMA show rapid changes of cloud cover during the second and third hour of simulation, respectively; and MOUM shows rapid rise of the centre of mass towards the end of the fourth hour of the simulation. In the final hour of the simulation, UKLEM shows too low a precipitation rate, too high a cloud cover, and too low a centre of mass of the cloud field, all consistent with the small horizontal domain applied (10 km $\times$ 10 km) which can hardly accommodate a single cumulonimbus. EULAG and MOUM show the highest centre of mass (around 8 and 9.5 km, respectively) towards the end of the simulations, which is perhaps consistent with relatively simple microphysical parametrizations applied by these models (note that the height of the centre of mass depends not only on the vertical cloud extent, but also on the vertical distribution of cloud condensate).

Except for GCE/1 km, the simulations shown in Figs. 13(b), 14(b) and 15(b) demonstrate a relatively good agreement with the benchmark. This is perhaps surprising for the SAM/500 m (cf. Petch *et al.* 2002), which has not only low horizontal resolution (500 m grid length) but also a relatively coarse vertical resolution (56 levels compared
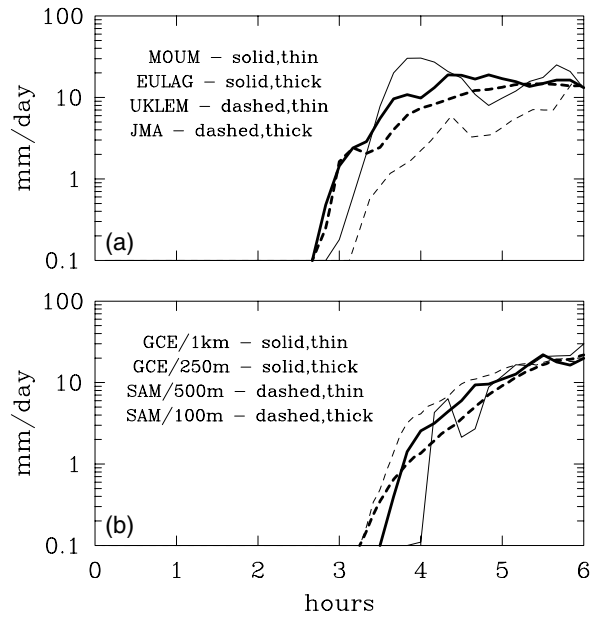
Figure 13.   Evolution of the surface precipitation rate for three-dimensional CRMs.
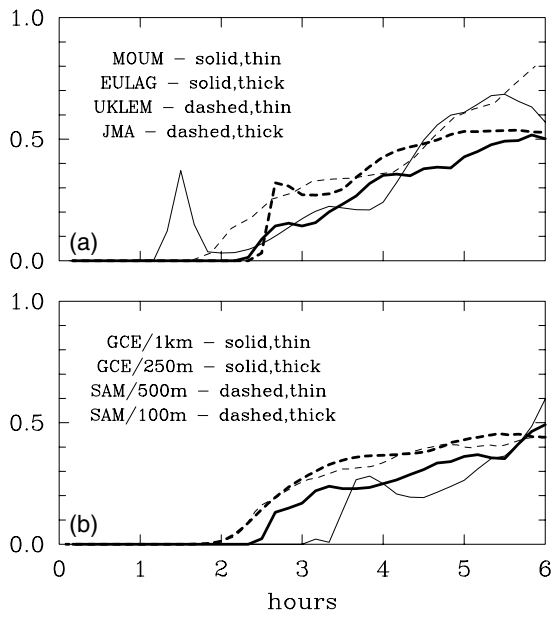

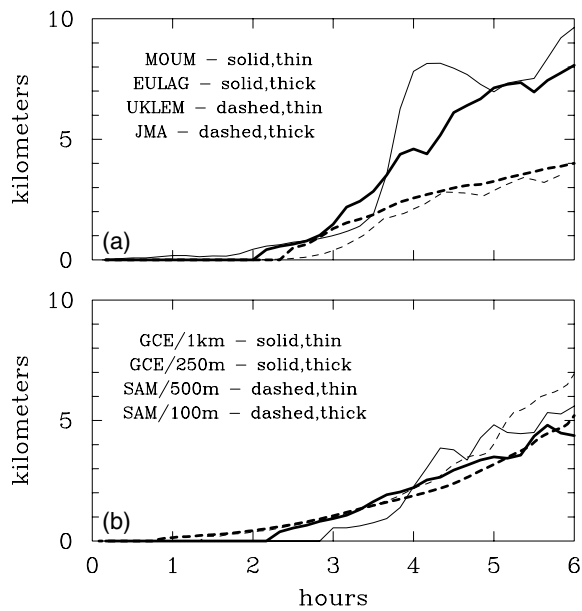Figure 14.   Evolution of cloud cover for three-dimensional CRMs.

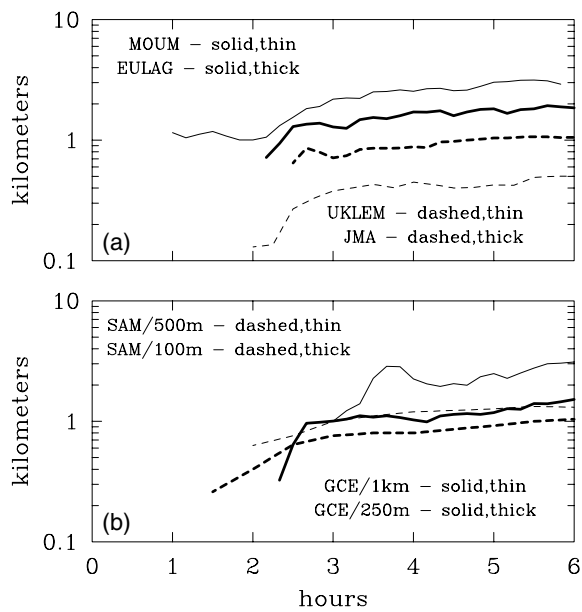Figure 15.   Evolution of height of the centre of mass of the cloud field for three-dimensional CRMs.

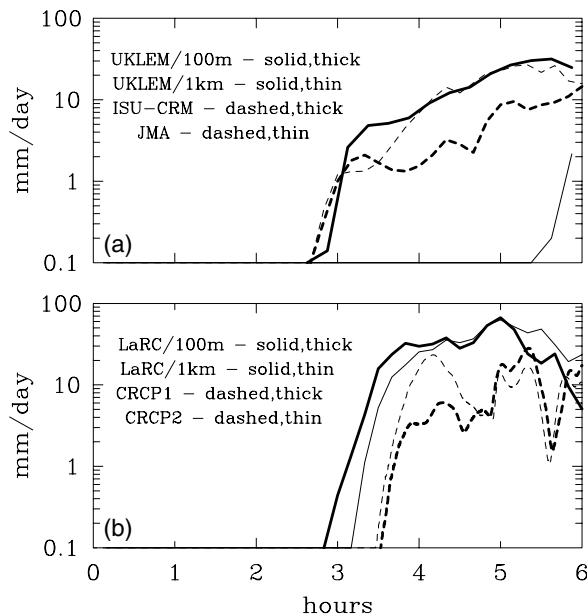Figure 16.   Evolution of mean cloud width for three-dimensional CRMs.

Figure 17. Evolution of the surface precipitation rate for two-dimensional CRMs.

to 256 levels in the high-resolution simulation). The fact that the low-resolution SAM model (which features only a standard Smagorinsky-type turbulence parametrization and no boundary-layer scheme) mimics high-resolution simulations (SAM/100 m and benchmark) is possibly due to the third-order time-integration scheme applied in this model. The diagnostic treatment of moist thermodynamics in SAM may also play a role. However, this is just a speculation which merits further investigation.

The mean cloud width (Fig. 16) increases in all simulations, but the evolution is different from the benchmark shown in Fig. 7. In most simulations, when clouds first appear their width is comparable to the horizontal grid length used in a given simulation. This is merely a reflection of the fact that clouds cannot be narrower than a few horizontal grid lengths if they result from the resolved dynamics. The SAM/100 m simulation shows values comparable to benchmark up to $t = 3$ h (except that it misses small clouds prior to $t = 1.5$ h), but the rate of increase of the cloud width is significantly slower after $t = 3$ h. Additional analysis of this simulation documents that the slow increase of the mean cloud width after $t = 3$ h results from a presence of a significant number of narrow and shallow clouds, together with clouds whose width and depth is more in line with the benchmark. This is supported by the comparison of the evolution of the height of the centre of mass in benchmark (Fig. 5) and in SAM/100 m (Fig. 15).

(b) 2D CRMs

As one may expect, two-dimensional simulations experienced more difficulties in representing the benchmark results. This is illustrated in Figs. 17 to 20, in the same format as for the 3D CRMs. Note that the figures include all 2D simulations listed in Table 3, and two CRCP simulations. The CRCP model includes random forcing that is different from all other CRMs and the two simulations are supposed to illustrate the impact of the random forcing (cf. Petch 2005).
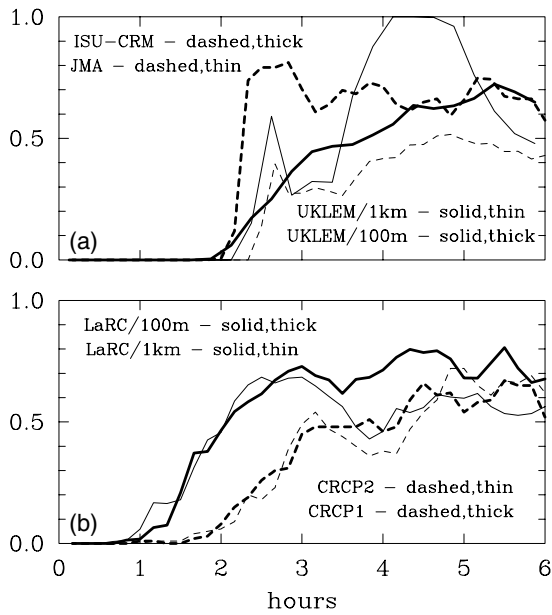
Figure 18.   Evolution of cloud cover for two-dimensional CRMs.
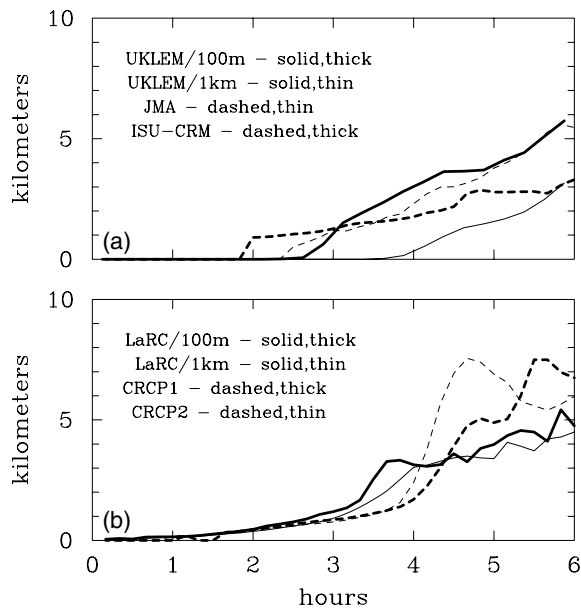

Figure 19.   Evolution of height of the centre of mass of the cloud field for two-dimensional CRMs.
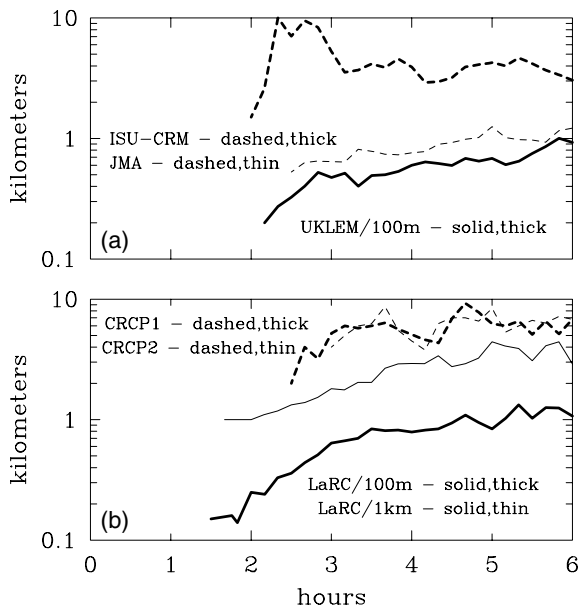
Figure 20. Evolution of mean cloud width for two-dimensional CRMs. The width for ISU-CRM is divided by 2 before plotting to fit the scale of the plot. Data for UKLEM/1 km is not shown as this simulation results is overcast conditions between hours 4 and 5 (cf. Fig. 18).

As demonstrated by Fig. 17, the surface precipitation rate in most 2D models reaches 0.1 mm d^{-1} around $t = 3$ h as well, except for UKLEM/1 km which does not reach this value until the last hour of the simulation. Figures 18 and 19 show that this simulation produces a shallow saturated cloud layer between hours 4 and 5 instead of deepening convection. The delay of convection initiation in this model is consistent with results discussed in Petch *et al.* (2002). In general, the increase of surface precipitation in all 2D models seems more rapid than in the benchmark (and similar to some lower-resolution 3D models, cf. Fig. 13), and the same seems true for the evolution of the cloud cover shown in Fig. 18.

Rapid increase of the cloud cover (Fig. 18) between hours 2 and 3 is most pronounced in simulations ISU-CRM, JMA and UKLEM/1 km. ISU-CRM applies a non-local boundary-layer parametrization. Without it, ISU-CRM is not capable of developing a realistic convective boundary layer in the first 3 h of the simulation and precipitation development is significantly delayed (not shown). This agrees with results of UKLEM/1 km which does not apply a boundary-layer scheme either. JMA uses higher horizontal resolution (grid length of 500 m), again without a boundary-layer scheme and the cloud cover also increases quite rapidly around $t = 2.5$ h.

The LaRC applies sophisticated boundary-layer parametrization (third-order closure) and forms clouds prior to $t = 1$ h, too early compared to the benchmark. Perhaps more significantly, the cloud cover increases quite rapidly between hours 1 and 3 and features values 2 to 3 times higher than the benchmark. This is consistent with the fact that the Sommeria–Deardorff subgrid-scale condensation scheme does not take into account subgrid-scale variability with non-zero skewness. It is well known that boundary-layer cumulus clouds are positively skewed (e.g. Cheng *et al.* 2004). Therefore, the overestimate of cloud cover is expected in the LaRC model with the Sommeria–Deardorff scheme. The differences between LaRC/100 m and LaRC/1 km are minor.

Cloud cover in CRCP increases at a slightly slower pace than in LaRC, but still too fast compared to the benchmark. Most simulations reproduce the gradual rise of the centre of mass of the cloud field (Fig. 19), but the scatter in both the rate of growth and the final height is significant. Fluctuations in the CRCP simulations, especially apparent in the evolution of the height of the centre of mass in the last two hours, illustrate the statistical uncertainty of the small-horizontal-domain 2D CRCP simulations.

The evolution of the mean cloud width (Fig. 20) supports the conclusions reached with 3D models, namely, that the initial cloud width reflects the model horizontal resolution and that the cloud width increases as the simulations progress. Fluctuations apparent in most simulations are a mere reflection of much smaller sample of clouds in 2D simulations at any given time. ISU-CRM simulates rapidly increasing cloud width during the third hour of the simulation and a gradual decrease thereafter. The latter is perhaps not surprising considering the low horizontal resolution applied by this model (grid length of 3 km).

7. DISCUSSION AND CONCLUSIONS

This paper discusses a model intercomparison case developed to investigate convective development over land and shallow to deep convection transition. The motivation for this study comes from the modelling results discussed in G2004 and B2004, where the entire diurnal cycle was simulated based on the observations at the ARM Southern Great Plains CART site. G2004 identified the period between sunrise and early afternoon local time as critical for the modelling of the entire diurnal cycle, with SCMs developing deep convection just a couple hours after the sunrise and missing the shallow convection phase (see also Betts and Jakob 2002a).

The case discussed herein is based on general features of convective development observed over Amazonia. The initial sounding, the evolution of surface latent- and sensible-heat fluxes, and the evolution of the temperature tendency due to radiative processes are all based on observations and simulations of the 23 February 1999 TRMM-LBA case. No large-scale advective tendencies of temperature or moisture are imposed. The case features the development of a well-mixed convective boundary layer from the early morning sounding, subsequent formation of shallow convection as the boundary layer deepens, and eventual transition from shallow to deep convection.

To faithfully represent the range of spatial scales involved and to provide a benchmark for other models, a custom-designed set of simulations applying increasing-in-time computational domain and decreasing spatial resolution was executed. These simulations were initiated using high spatial resolution and small computational domain typical of large-eddy simulations (LES) applied in boundary-layer studies. To reach a computational domain large enough for deep convection (both in the horizontal and in the vertical), an approach similar to that applied by Müller and Chlond (1996) in their simulation of the boundary-layer development in cold-air outbreaks was used. In this approach, a remapping procedure was applied three times to increase the computational domain and horizontal/vertical grid length towards those applied in CRM simulations.

The benchmark simulations documented development of the convective boundary layer as the surface fluxes increase after sunrise and predicted the formation of small clouds (around 200 m wide) near the boundary-layer top after just about an hour of the simulation. In the subsequent two hours, boundary-layer depth, the depth of convection layer, and the mean cloud width were gradually increasing, reaching about 500 m, 2 km and 1 km for boundary-layer depth, top of the convection layer, and cloud width, respectively, at $t = 3$ h. At about this time, the model predicted a trace

of surface precipitation (domain-averaged rate of 0.1 mm day^{-1}). During the following two hours (between $t = 3$ and 5 h), the depth of clouds continued to increase, reaching the upper troposphere by $t = 5$ h. At this time, the mean cloud width was around 3 km and the mean surface precipitation about 10 mm d^{-1}. The latter was comparable to the maximum surface precipitation during the diurnal cycle (in the range of 40 to 60 mm d^{-1} during the rainy season, e.g. Rickenbach *et al.* (2002), Fig. 12). The cloud-base upward mass flux was in the range of 0.1 to 0.2 kg m^{-2}s^{-1} and did not change significantly as the convection went through transition from shallow to deep. As expected, the cloud downdraught mass fluxes reached magnitudes comparable to updraught mass fluxes only after significant precipitation developed at around $t = 5$ h. The simulations were truncated at $t = 6$ h (1330 LST) and did not investigate mesoscale organization in the afternoon and gradual transition from convection-dominated to stratiform-dominated precipitation during the late afternoon and evening hours.

While simulating this case, the two SCMs experienced similar problems to those highlighted in Betts and Jakob (2002a), B2004 and G2004. Deep convection developed during the second hour of the simulation, a few hours too early compared to the benchmark, essentially bypassing the shallow convection phase. This occurred despite the fact that the development of a well-mixed boundary layer was quite realistically represented by both models. Benchmark simulations suggest a possible path to improve the behaviour of the SCMs because the gradual increase of the cloud depth was accompanied by the similar increase of the mean cloud width. Since the entrainment coefficient (whose magnitude has a strong impact on the depth of the convection layer) is inversely proportional to the cloud width, perhaps a more gradual deepening of the parametrized convection can be obtained by applying a decreasing entrainment coefficient as the day progresses, from large values typical for shallow convection to an order of magnitude smaller values typical for deep convection. Simple tests of such an approach can be performed using the test case discussed in this paper and such tests will be reported in the future.

The CRMs were capable of capturing the qualitative aspects of the daytime convective development, but there were significant differences among the models. As far as 3D CRMs are concerned, a horizontal grid length around 500 m seems sufficient to capture essential processes involved in convective development. Of course, very small clouds (smaller than 1 km as in the second hour of the benchmark simulation) cannot be captured with such a low spatial resolution and thus some delay in formation of first clouds is unavoidable. Whether this delay is important from the point of view of the surface energy budget requires further investigation (see later). Some 3D models appear to perform better than others even when the exact same spatial resolution is applied. This may be a function of particular subgrid-scale parametrizations applied, but may also depend on seemingly minor details of the modelling set-up (e.g. amplitude of the random noise applied throughout the simulation, cf. Petch (2005)). Investigation of those aspects is beyond the scope of this preliminary study.

The above conclusions apply to the 2D CRMs to a lesser degree. Two-dimensional models simulate too rapid a transition from shallow to deep convection (e.g. the surface precipitation rate increases more rapidly than in benchmark) and a more rapid increase of the cloud cover after initial formation of clouds (compared to benchmark and to 3D simulations). Again, the impact of these deviations on the surface energy budget needs to be investigated in a follow-up study where several diurnal cycles are considered as in Betts and Jakob (2002b) and G2004. Such a new multi-day case using an interactive radiation transfer model and a simple land surface model is currently being developed by the lead author of this paper and the results will be presented in the future.

An important issue is the generality of the results discussed in this paper in terms of convective development over different geographical regions. For instance, G2004 and B2004 argue that the shallow convection phase played an important role in moistening the lower troposphere prior to the deep convection onset. This aspect, noticeable in Fig. 4, is not expected to play a significant role in the LBA case because of the very humid initial sounding. Perhaps more important is the role of the surface flux partitioning between sensible- and latent-heat flux which, for instance, is different over the ARM site (cf. Brown *et al.* 2002; G2004). Since the flux partitioning affects the rate of growth of the boundary layer, some modifications of the picture discussed in this paper are expected. However, the overall pattern is likely to be similar.

Finally, the analysis presented in this paper merely scratches the surface as far as the analysis of factors involved in the modelling of convective development over land is concerned. These will be discussed in upcoming papers by individual modellers involved in this initial study.

APPENDIX

Forcing data for model simulations

The initial sounding is given in Table A.1. Evolution of surface sensible F_S and latent F_L heat fluxes (W m^{-2}) is given by:

$$F_S = 270 \times f(t)^{1.5}, \tag{A.1}$$

$$F_L = 554 \times f(t)^{1.3}, \tag{A.2}$$

where

$$f(t) = \max\left\{0, \cos\left(\frac{\pi}{2}\frac{5.25 - t}{5.25}\right)\right\},$$

with t being the model simulation time in hours (i.e. from 0 to 6 h). This formula gives vanishing surface fluxes at $t = 0$, and a maximum of 270/554 W m^{-2} of sensible/latent fluxes at $t = 5.25$ h of the simulation.

The evolution of the temperature tendency due to radiative processes is shown in Fig. A.1. The data come from CRM simulation of this case by S. Lang and W.-K. Tao using the interactive radiation transfer model. The data and additional comments are available at http://box.mmm.ucar.edu/gcss-wg4/gcss/case4.html.

TABLE A.1. INITIAL SOUNDING

Height (km)	Pressure (hPa)	Temperature (°C)	RH (%)	U (m s^{-1})	V (m s^{-1})
0.130	991.3	23.70	98.00	0.00	−0.40
0.464	954.2	23.30	86.00	0.81	−3.51
0.573	942.0	22.57	88.56	1.17	−3.88
1.100	886.9	19.90	87.44	3.44	−4.77
1.653	831.5	16.91	86.67	3.53	−5.28
2.216	778.9	14.09	83.67	3.88	−5.85
2.760	729.8	11.13	79.56	4.09	−5.60
3.297	684.0	8.29	84.78	3.97	−2.67
3.824	641.7	5.38	84.78	1.22	−1.47
4.327	603.2	2.29	89.33	0.16	0.57
4.787	570.1	−0.66	94.33	−1.22	0.89
5.242	538.6	−3.02	92.00	−1.72	−0.08
5.686	509.1	−5.28	85.22	−2.77	1.11
6.131	480.4	−7.42	77.33	−2.65	2.15
6.578	454.0	−10.34	80.11	−0.64	3.12
6.996	429.6	−12.69	66.11	−0.07	3.22
7.431	405.7	−15.70	72.11	−1.90	3.34
7.881	382.5	−19.21	72.67	−2.70	1.91
8.300	361.1	−21.81	52.22	−2.99	1.15
8.718	340.9	−24.73	54.67	−3.66	1.01
9.149	321.2	−27.76	51.00	−5.05	−0.57
9.611	301.2	−30.93	43.78	−6.64	−0.67
10.084	281.8	−34.62	40.56	−4.74	0.31
10.573	263.1	−38.58	43.11	−5.30	2.97
11.008	246.1	−42.30	54.78	−6.07	2.32
11.460	230.1	−46.07	46.11	−4.26	2.66
11.966	213.2	−50.03	42.33	−7.52	4.79
12.472	197.0	−54.67	43.22	−8.88	3.40
12.971	182.3	−59.16	45.33	−9.00	3.14
13.478	167.9	−63.60	39.78	−7.77	3.93
13.971	154.9	−67.68	33.78	−5.37	7.57
14.443	143.0	−70.77	28.78	−3.88	2.58
14.956	131.1	−74.41	24.67	−1.15	2.50
15.458	119.7	−77.51	20.67	−2.36	6.44
16.019	108.9	−80.64	17.67	−9.20	6.84
16.491	100.1	−80.69	17.11	−8.01	0.19
16.961	92.1	−80.00	16.22	−5.68	−2.20
17.442	84.6	−81.38	14.22	−8.83	−3.60
17.934	77.5	−81.17	13.00	−14.51	0.56
18.397	71.4	−78.32	13.00	−15.55	6.68
18.851	65.9	−74.77	12.22	−15.36	9.41
19.331	60.7	−74.52	9.56	−17.67	7.03
19.809	55.9	−72.62	7.78	−17.82	5.32
20.321	51.3	−70.87	5.89	−18.94	1.14
20.813	47.2	−69.19	4.33	−15.92	−0.65
21.329	43.3	−66.90	3.00	−15.32	5.27
30.000	10.3	−66.90	3.00	−15.32	5.27

RH = relative humidity; U/V = zonal/meridional velocity component. Note that height represents height above sea level, with the first level (130 m) provided. Model results are shown using height above the surface as vertical coordinate.
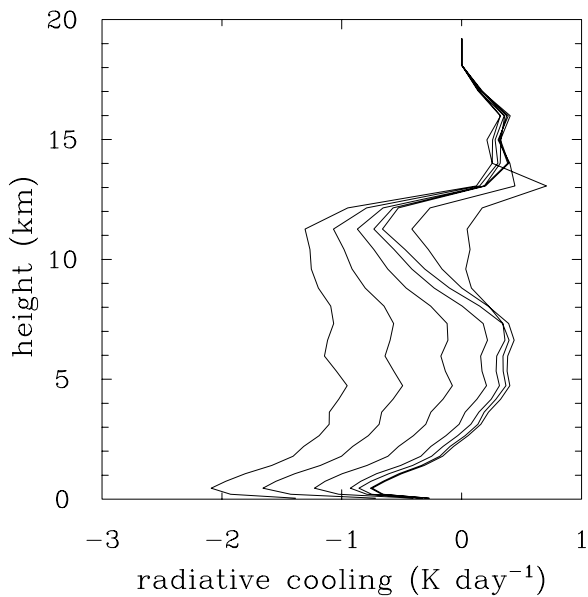
Figure A.1.   Evolution of the radiative cooling applied in the simulations. The leftmost line is for $t = 0$, and the subsequent lines towards the right show tendencies for $t = 1, 2, 3$ etc. hours.

REFERENCES

Anderson, W. D., Grubišić, V. and Smolarkiewicz P. K.   1997   'Performance of a massively parallel 3D non-hydrostatic atmospheric fluid model'. Pp. 645–651 in Proceedings of the international conference on parallel and distributed processing techniques and applications. Ed. H. R. Arabnia, Computer Science Research, Education, and Application Tech (CSREA). (Available from Dr. P. K. Smolarkiewicz, NCAR, PO Box 3000, Boulder, CO 80307)

Bechtold, P., Chaboureau, J.-P., Beljaars, A., Betts, A. K., Köhler, M., Miller, M. and Redelsperger, J.-L.   2004   The simulation of the diurnal cycle of convective precipitation over land in a global model. *Q. J. R. Meteorol. Soc.*, **131,** 3119–3137

Betts, A. K. and Jakob, C.   2002a   Evaluation of the diurnal cycle of precipitation, surface thermodynamics, and surface fluxes in the ECMWF model using LBA data. *J. Geophys. Res.*, **107**(D20)**,** doi: 10.1029/2001JD000427

    2002b   Study of diurnal cycle of convective precipitation over Amazonia using a single column model. *J. Geophys. Res.*, **107**(D23)**,** doi: 10.1029/2002JD002264

Betts, A. K., Fuentes, J. D., Garstang, M. and Ball, J. H.   2002   Surface diurnal cycle and boundary layer structure over Rondonia during rainy season. *J. Geophys. Res.*, **107**(D20)**,** doi: 10.1029/2001JD000356

Brown, A. R., Cederwall, R. T., Chlond, A., Duynkerke, P. G., Golaz, J.-C., Khairoutdinov, M., Lewellen, D. C., Lock, A. P., MacVean, M. K., Moeng, C.-H., Neggers, R. A. J., Siebesma, A. P. and Stevens, B.   2002   Large-eddy simulation of the diurnal cycle of shallow convection over land. *Q. J. R. Meteorol. Soc.*, **128,** 1075–1094

Cheng, A., Xu, K.-M. and Golaz, J.-C.   2004   The liquid-water oscillation in modeling boundary-layer cumuli with third-order turbulence closure models. *J. Atmos. Sci.*, **61,** 1621–1629

Clark T. L., Hall, W. D. and Coen, J. L.	1996	Source code documentation for the Clark–Hall cloud-scale model: Code version G3CH01. NCAR Technical Note, NCAR/TN–426+STR
Davies, T. D., Cullen, M. J. P., Malcolm, A. J., Mawson, M. H., Staniforth, A., White, A. A. and Wood, N.	2005	A new dynamical core for the Met Office's global and regional modelling of the atmosphere. *Q. J. R. Meteorol. Soc.*, **131,** 1759–1782
Grabowski, W. W.	1998	Toward cloud resolving modeling of large-scale tropical circulations: A simple cloud microphysics parameterization. *J. Atmos. Sci.*, **55,** 3283–3298
	2001	Coupling cloud processes with the large-scale dynamics using the cloud-resolving convection parameterization (CRCP). *J. Atmos. Sci.*, **58,** 978–997
	2003	MJO-like coherent structures: Sensitivity simulations using the cloud-resolving convection parameterization (CRCP). *J. Atmos. Sci.*, **60,** 847–864
Grabowski, W. W. and Smolarkiewicz, P. K.	1996	On two-time-level semi-Lagrangian modeling of precipitating clouds. *Mon. Weather Rev.*, **124,** 487–497
Gregory, D. and Rowntree, P. R. R.	1990	A mass flux convection scheme with representation of cloud ensemble characteristics and stability dependent closure. *Mon. Weather Rev.*, **118,** 1483–1506
Guichard, F., Petch, J. C., Redelsperder, J.-L., Bechtold, P., Chaboureau, J.-P., Cheinet, S., Grabowski, W., Grenier, H., Jones, C. G., Köhler, M., Piriou, J.-M., Tailleax, R. and Tomasini, M.	2004	Modelling the diurnal cycle of deep precipitating convection over land with cloud-resolving models and single-column models. *Q. J. R. Meteorol. Soc.*, **131,** 3139–3172
Ikawa, M., Mizuno, H., Matsuo, T., Murakami, M., Yamada, Y. and Saito, K.	1991	Numerical modeling of the convective snow cloud over the Sea of Japan: Sensitivity to ice crystal nucleation rates. *J. Meteorol. Soc. Jpn*, **69,** 641–667
Khairoutdinov, M. F. and Randall, D. A.	2003	Cloud-resolving modeling of the ARM summer 1997 IOP: Model formulation, results, uncertainties and sensitivities. *J. Atmos. Sci.*, **60,** 607–625
Krueger, S. K.	1988	Numerical simulation of tropical cumulus clouds and their interaction with the subcloud layer. *J. Atmos. Sci.*, **45,** 2221–2250
Lock, A. P., Brown, A. R., Bush, M. R., Martin, G. M. and Smith, R. N. B.	2000	A new boundary layer mixing scheme. Part I. Scheme description and single-column model tests. *Mon. Weather Rev.*, **128,** 3187–3199
Müller, G. and Chlond, A.	1996	Three-dimensional numerical study of cell broadening during cold-air outbreaks. *Boundary-Layer Meteorol.*, **81,** 298–323
Petch, J. C.	2005	The predictability of convection in cloud-resolving simulations over land. *Q. J. R. Meteorol. Soc.*, **131,** 3173–3187
Petch, J. C., Brown, A. R. and Gray, M. E. B.	2002	The impact of horizontal resolution on the simulations of convective development over land. *Q. J. R. Meteorol. Soc.*, **128,** 2031–2044
Pope, V. D., Gallani, M., Rowntree, P. R. and Stratton, R. A.	2000	The impact of new physical parametrizations in the Hadley Centre climate model HadAM3. *Clim. Dyn.*, **16,** 123–146
Rickenbach, T. M., Nieto Ferreira, R., Halverson, J. B., Herdies, D. L. and Silva Dias, M. A. F.	2002	Modulation of convection in southwestern Amazon basin by extratropical stationary fronts. *J. Geophys. Res.*, **107**(D20)**,** doi: 10.1029/2000JD000263
Saito, K.	1993	A numerical study of the local downslope wind 'Yamaji-kaze' in Japan. Part 2: Non-linear aspect of the 3-D flow over a mountain range with a col. *J. Meteorol. Soc. Jpn*, **71,** 247–271
Saito, K., Kato, T., Eito, H. and Muroi, C.	2001	Documentation of the Meteorological Research Institute/Numerical Prediction Division Unified Nonhydrostatic Model. *Tech. Pep. MRI*, **42**
Shutts, G. J. and Gray, M. E. B.	1994	A numerical modeling study of the geostrophic adjustment process following deep convection. *Q. J. R. Meteorol. Soc.*, **120,** 1145–1178
Smolarkiewicz, P. K. and Grabowski, W. W.	1990	The multidimensional positive advection transport algorithm: Nonoscillatory option. *J. Comput. Phys.*, **86,** 355–375

Smolarkiewicz, P. K. and Margolin, L. G. 1997 On forward-in-time differencing for fluids: An Eulerian/semi-Lagrangian nonhydrostatic model for stratified flows. *Atmos.–Ocean Special*, **35,** 127–152

Sommeria, G. and Deardorff, J. W. 1977 Subgrid-scale condensation in models of non-precipitating clouds. *J. Atmos. Sci.*, **34,** 344–355

Swann, H. 1998 Sensitivity to the representation of precipitating ice in CRM simulations of deep convection. *Atmos. Res.*, **48,** 415–435

Tao, W.-K. and Simpson, J. 1993 Goddard Cumulus Ensemble Model. Part I: Model description. *Terrestrial, Atmospheric and Oceanic Sciences*, **4,** 35–72

Tao, W.-K., Simpson, J., Baker, D., Braun, S., Chou, M.-D., Ferrier, B., Johnson, D., Khain, A., Lang, S., Lynn, B., Shie, C.-L., Starr, D., Sui, C.-H., Wang, Y. and Wetzel, P. 2003 Microphysics, radiation and surface processes in the Goddard Cumulus Ensemble (GCE) model. *Meteorology and Atmospheric Physics*, **82,** 97–137

Tiedtke, M. 1989 A comprehensive mass flux scheme for cumulus parameterization in large-scale models. *Mon. Weather Rev.*, **117,** 1779–1800

Troen, I. and Mahrt, L. 1986 A simple model of the atmospheric boundary layer; sensitivity to surface evaporation. *Boundary-Layer Meteorol.*, **37,** 129–148

Wilson, D. R. and Ballard, S. P. 1999 A microphysically based precipitation scheme for the UK Meteorological Office Unified Model. *Q. J. R. Meteorol. Soc.*, **125,** 1607–1636

Wu, X. and Moncrieff, M. W. 2001 Long-term behavior of cloud systems in TOGA COARE and their interactions with radiative and surface processes. Part III: Effects on the energy budget and SST. *J. Atmos. Sci.*, **58,** 1155–1168

Xie, S.-C., Xu, K.-M., Cederwall, R. T., Bechtold, P., Del Genio, A. D., Klein, S. A., Cripe, D. G., Ghan, S. J., Gregory, D., Iacobellis, S. F., Krueger, S. K., Lohmann, U., Petch, J. V., Randall, D. A., Rotstayn, L. D., Somerville, R. C. J., Sud, Y. C., von Salzen, K., Walker, G. K., Wolf, A., Yio, J. J., Zhang, G. J. and Zhang, M. 2002 Intercomparison and evaluation of cumulus parametrizations under summertime midlatitude continental conditions. *Q. J. R. Meteorol. Soc.*, **128,** 1095–1135

Xu, K.-M. and Krueger, S. K. 1991 Evaluation of cloudiness parameterizations using a cumulus ensemble model. *Mon. Weather Rev.*, **119,** 342–367

Yang, G.-Y. and Slingo, J. 2001 The diurnal cycle in the tropics. *Mon. Weather Rev.*, **129,** 784–801